Bai, L., Velichko, A., & Drinkwater, B. W. (2018). Ultrasonic defect characterisation-Use of amplitude, phase, and frequency information. *Journal of the Acoustical Society of America*, *143*(1), 349-360. https://doi.org/10.1121/1.5021246

Ultrasonic defect characterisation—Use of amplitude, phase, and frequency information

Long Bai, Alexander Velichko, and Bruce W. Drinkwater

Citation: The Journal of the Acoustical Society of America **143**, 349 (2018); doi: 10.1121/1.5021246
View online: https://doi.org/10.1121/1.5021246
View Table of Contents: http://asa.scitation.org/toc/jas/143/1
Published by the Acoustical Society of America

Ultrasonic defect characterisation—Use of amplitude, phase, and frequency information

Long Bai,[a] Alexander Velichko, and Bruce W. Drinkwater
Department of Mechanical Engineering, University of Bristol, Bristol BS8 1TR, United Kingdom

(Received 6 October 2017; accepted 22 December 2017; published online 23 January 2018)

This paper studies ultrasonic defect characterisation with the aim of reducing the characterisation uncertainty. Ultrasonic array data contain a mixture of responses from all reflecting features, and the scattering matrix for each defect can be extracted in post-processing, which describes how ultrasonic waves at a given incident angle are scattered by a defect. In this paper, it is shown that defect characterisation performance can be improved by the inclusion of phase and frequency information relative to current single-frequency-amplitude approaches. This superior characterisation performance is due to the increased number of informative principal components (PCs) and higher signal-to-noise ratios in the PC directions. Scattering matrix phase measurement is very sensitive to localisation errors, and an effective approach is proposed, which can be used to reliably extract phase from experimental data. Nine elliptical defects having different aspect ratios and orientation angles are characterised experimentally. The complex multi-frequency defect database has achieved up to 90.60% reduction in the quantified sizing uncertainty compared to the results obtained using only the amplitude at a single frequency.

https://doi.org/10.1121/1.5021246

[KGS] Pages: 349–360

I. INTRODUCTION

Defect characterisation is one of the main objectives of ultrasonic non-destructive evaluation,[1–3] and helps to provide critical information on structural integrity.[4] Accurate defect characterisation requires both the defect type (often related to the severity of a defect) and defect parameters (e.g., size and orientation) to be determined from a given measurement. Considerable efforts have been reported in the literature for the characterisation of crack-like defects,[5–9] volumetric defects and inclusions,[10–13] and porosity.[14–16] The proposed approaches were mainly developed for a given type of defect. For example, the size of crack-like defects was determined by measuring the scattering amplitude or using the so-called 6 dB drop approach.[5] Surface-breaking cracks were sized by measuring the tip diffracted signals.[6] Inverse Born approximation was used to reconstruct voids and inclusions.[12] When applying the reconstruction algorithm, similarly to the 6 dB drop approach, the effective radius of a defect was defined to be the distance at which the characteristic function drops by one-half from its maximum value.[12]

Ultrasonic transducer arrays have been increasingly used for detection and characterisation of defects in recent decades due to their increased flexibility over traditional single element transducers.[17,18] The ultrasonic imaging capability has been significantly improved with the help of post-processing algorithms such as the total focusing method[19] and the inverse wave field extrapolation (IWEX) method,[20] which makes it possible to characterise defects directly from their images.[21,22] Alternatively, the far-field angular scattering pattern of a defect can be measured and used for defect characterisation. The array data measured from all possible combinations of transmitter and receiver elements can be used to extract this information, which is often represented in the form of a scattering matrix.[21] It is rational to use the scattering matrix in defect characterisation, since it encodes all the defect information, which is extractable from an array measurement.[11] Database search approaches have been proposed in which scattering matrix databases were formed using modeled data for ideal reference defects.[9,11] These approaches were recently generalised with the introduction of the defect manifold, and an approach to quantifying the characterisation uncertainty was proposed.[23] The scattering matrix was also used in an inversion process where the defect geometry is updated in iterations until a satisfactory match is achieved between the modeled data and the measurement.[10]

Defect characterisation based on the scattering matrix was shown to be particularly effective for relatively small defects.[9,11,21] It was also concluded that the sensitivity of the scattering matrix to the defect size becomes lower as the defect size exceeds 2λ.[21] Another major limitation of the previous approaches arises for difficult measurement scenarios where the accessible region of a component is limited due to geometrical restrictions, and for unfavourably oriented defects from which the most distinctive scattering information (i.e., the specular reflection) is unmeasurable. The lack of useful characterisation information can potentially lead to large characterisation errors, and is often related with high characterisation uncertainty.[23] Since previous approaches only make use of the amplitude of a scattering matrix, it is noted that these limitations can be addressed by using additional information (i.e., the phase part of a

[a]Electronic mail: lb13340@bristol.ac.uk

scattering matrix). In addition, as the scattering matrix varies with the frequency, using the scattering data obtained at multiple frequencies is also expected to be beneficial.

The main purpose of this paper is to investigate the possibility of using the phase information of a scattering matrix reliably for more accurate defect characterisation, and to study the performance improvement by using scattering matrix at multiple frequencies. In Sec. II, scattering matrix databases with and without phase are compared, and it is shown that relatively large defects can be characterised with significantly reduced uncertainty by using the phase information. The effect of localisation error on the measured phase of a scattering matrix is investigated in Sec. III, where an efficient approach to addressing this issue is proposed. The experimental results are discussed in Sec. IV.

II. THE SCATTERING MATRIX DATABASES WITH AND WITHOUT PHASE

A. Defect characterisation problem and the defect manifold

Defects can have different shapes in a structure, and in order to accurately characterise them using an inversion procedure, scattering data of different types of defects need to be modeled in forward simulations. In this paper, the scattering data of a defect are represented in the form of a far-field scattering matrix, which is defined as (assuming a two-dimensional geometry of the defect)[11]

$$\boldsymbol{S}(\theta_1,\theta_2,\omega)=\frac{a_{\mathrm{sc}}(\omega)}{a_{\mathrm{in}}(\omega)}\sqrt{\frac{d_{\mathrm{sc}}}{\lambda}}\exp\left(-\frac{i\omega d_{\mathrm{sc}}}{c}\right). \tag{1}$$

In Eq. (1), θ_1,θ_2 are the incident and scattering angles (see Fig. 1), respectively, a_{in} is the amplitude of the plane incident wave, a_{sc} is the amplitude of the scattered wave, which is measured at a distance d_{sc} from the defect, λ is the ultrasonic wavelength, c is the speed of ultrasonic waves, and ω is the angular frequency. The scattering matrix database is constructed using the scattering matrices of reference defects including cracks, holes, and ellipses. When calculating the scattering matrix of a reference crack, the far-field asymptotic solution given by Glushkov *et al.*[24] is adopted. For ellipses and holes, a finite element local scattering (FELS) model[25] is used to simulate the scattering matrices. Figure 1 shows the measurement configuration adopted in simulation. The incident and scattering angles are defined with respect to the array normal, and are positive if measured clockwise. The material modeled in simulation is aluminum (Young's modulus = 69 GPa, Poisson's ratio = 0.334, and density = 2700 kg/m^3).

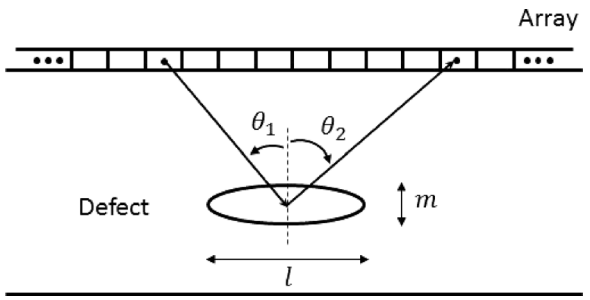

FIG. 1. Measurement configuration adopted in simulation.

For ellipses, a critical parameter that describes the defect geometry is the aspect ratio, which is defined as the ratio of the minor axis (m in Fig. 1) to the major axis (l in Fig. 1). Following this definition, it is straightforward to assign aspect ratios of 0 and 1 to cracks and holes, respectively. As is shown in Fig. 1, defects are assumed to be horizontal in simulation, and hence, the defect geometry can be described using two parameters: size l and aspect ratio r. However, it should be pointed out that the applicability of the scattering matrix database is not affected by the dimensionality of the defect parameters. A more general situation is considered in Sec. IV, where the orientation angle of a defect is introduced as a third defect parameter.

The scattering matrices in the database are simulated for incident and scattering angles between $-90°$ and $90°$, which represent the maximum amount of information extractable from a one-sided measurement. The forward simulations are performed at the centre frequency of 2.5 MHz, and the considered size range is between 0.5λ (i.e., 1.25 mm) and 3λ (i.e., 7.5 mm). The aspect ratio range of the defect database is between 0 (i.e., cracks) and 1 (i.e., holes) as explained above. The sampling intervals of defect size and aspect ratio are selected to be 0.1λ (i.e., 0.25 mm) and 0.05, respectively. Hence, the total number of reference defects in the database is 26 (number of sizes)×21 (number of aspect ratios)=546.

Four different versions of the scattering matrix database are compared in this section. Database 1 is constructed using only the amplitude of a scattering matrix, which is simulated at the centre frequency. The scattering matrices in database 2 are also simulated at the centre frequency, but include both the amplitude and phase information (organised in the form of real and imaginary parts). Databases 3 and 4 contain scattering matrices simulated at multiple frequencies (i.e., 1.5 MHz, 2 MHz, 2.5 MHz, 3 MHz, and 3.5 MHz). Database 3 includes only the amplitude of the scattering matrices, whereas database 4 includes both the amplitude and phase information. Hence, the same scattering matrix $\boldsymbol{S}$ (of a reference defect) is included in the four databases in the forms given by

$$\boldsymbol{S}^{(\mathrm{db},1)}=|\boldsymbol{S}(\omega_c)|^T, \tag{2}$$

$$\boldsymbol{S}^{(\mathrm{db},2)}=[\mathrm{Re}\{\boldsymbol{S}(\omega_c)\},\mathrm{Im}\{\boldsymbol{S}(\omega_c)\}]^T, \tag{3}$$

$$\boldsymbol{S}^{(\mathrm{db},3)}=[|\boldsymbol{S}(\omega_i)|]^T,\quad i=1,2,3,4,5. \tag{4}$$

$$\boldsymbol{S}^{(\mathrm{db},4)}=[\mathrm{Re}\{\boldsymbol{S}(\omega_i)\},\mathrm{Im}\{\boldsymbol{S}(\omega_i)\}]^T,\quad i=1,2,3,4,5. \tag{5}$$

In Eqs. (2)–(5), ω_c is the angular frequency corresponding to the centre frequency of 2.5 MHz, and ω_i ($i=1,2,3,4,5$) are the angular frequencies corresponding to the frequencies 1.5 MHz, 2 MHz, 2.5 MHz, 3 MHz, and 3.5 MHz, respectively. The arguments θ_1 and θ_2 of the scattering matrix are omitted for simplicity, whose ranges are the same (i.e., between $-90°$ and $90°$) for all the databases. $\mathrm{Re}\{\boldsymbol{S}\}$ and $\mathrm{Im}\{\boldsymbol{S}\}$ are real and imaginary parts, respectively, of the scattering matrix $\boldsymbol{S}$, and can be obtained as

$$\mathrm{Re}\{\boldsymbol{S}\} = |\boldsymbol{S}|\cos[\Phi(\boldsymbol{S})], \quad \mathrm{Im}\{\boldsymbol{S}\} = |\boldsymbol{S}|\sin[\Phi(\boldsymbol{S})], \tag{6}$$

where $\Phi(\boldsymbol{S})$ denotes the phase of the scattering matrix $\boldsymbol{S}$.

Data in each scattering matrix database can be used to construct a defect manifold (or d-manifold),[23] which is a representation of the database in principal component space (or pc-space) and contains "the entirety of the characterisation information" for the given types of defects.[23] Principal component analysis (PCA)[26] is applied to the databases, which helps to reduce their dimensionality. For the purpose of PCA, a scattering matrix database is shifted in amplitude to have zero mean, and can be written as

$$\boldsymbol{T}_j = \left[\boldsymbol{S}_1^{(\mathrm{db},j)} - \bar{\boldsymbol{S}}^{(\mathrm{db},j)}, \boldsymbol{S}_2^{(\mathrm{db},j)} - \bar{\boldsymbol{S}}^{(\mathrm{db},j)}, \ldots, \boldsymbol{S}_M^{(\mathrm{db},j)} - \bar{\boldsymbol{S}}^{(\mathrm{db},j)}\right], \quad j = 1,2,3,4, \tag{7}$$

where $\boldsymbol{S}_i^{(\mathrm{db},j)}$ $(i = 1,2,\ldots,M,\ j = 1,2,3,4)$ is the scattering matrix of a reference defect, which is prepared in one of the forms given in Eqs. (2)–(5), $\bar{\boldsymbol{S}}^{(\mathrm{db},j)}$ $(j = 1,2,3,4)$ is the mean scattering matrix of database j, and $M(= 546)$ is the total number of the reference defects. Then, the covariance matrices of the databases can be obtained as

$$\boldsymbol{R}_j = \frac{1}{M-1}\boldsymbol{T}_j\boldsymbol{T}_j^T, \quad j = 1,2,3,4. \tag{8}$$

Eigendecomposition of $\boldsymbol{R}_j$ gives the new coordinate system, which defines the pc-space

$$\boldsymbol{R}_j = \boldsymbol{V}_j\boldsymbol{D}_j\boldsymbol{V}_j^T, \quad j = 1,2,3,4. \tag{9}$$

In Eq. (9), $\boldsymbol{D}_j$ $(j = 1,2,3,4)$ is a diagonal matrix containing the eigenvalues of the matrix $\boldsymbol{R}_j$, and columns of $\boldsymbol{V}_j$ are the coordinate axes of the pc-space. This effectively reduces the dimensionality of the scattering matrix database because the first few eigenvalues (i.e., the diagonal elements of $\boldsymbol{D}_j$) are significantly larger than the rest.[23] The number of the informative eigenvectors, N_{PC}, can be determined by selecting some threshold d_0, and eigenvectors that are associated with eigenvalues above the threshold are retained. In this paper, d_0 is set to be $0.01 \times d_{1,j}$, where $d_{1,j}$ is the first (i.e., the largest) eigenvalue of database j. After PCA, the scattering matrix $\boldsymbol{S}_i^{(\mathrm{db},j)}$ is transformed into the pc-space by

$$\boldsymbol{P}_i^{(\mathrm{db},j)} = \mathrm{V}_j'^T(\boldsymbol{S}_i^{(\mathrm{db},j)} - \bar{\boldsymbol{S}}^{(\mathrm{db},j)}), \quad j = 1,2,3,4, \tag{10}$$

where $\boldsymbol{V}_j'$ consists of the first N_{PC} columns of the matrix $\boldsymbol{V}_j$.

Figures 2(a)–2(d) show the shapes of the d-manifolds of databases 1–4 in three-dimensional pc-space, and Fig. 2(e) shows a two-dimensional space that defines the domain of the defect parameters. Note that each point on the d-manifold can be parametrically described by the parameters l and r, and a color map defined in Fig. 2(e) is used to explicitly show the mapping between points in parameter space and pc-space. Compared to databases 2 and 4, the d-manifolds of databases 1 and 3 (i.e., include only the amplitude of the scattering matrix) have simpler geometries, which are well correlated with the parameter space (e.g., points located at different local regions of the parameter space are also well separated in pc-space). However, it should be noted that this is because of the fact that the d-manifolds of databases 1 and 3 have lower dimensionality than those of databases 2 and 4 in pc-space, and hence, are better visualised in three dimensions. For example, the ranges of "PC 2" and "PC 3" (i.e., the second and third principal components, or PCs) shown in Figs. 2(b) and 2(d) are similar to the range of "PC 1" (i.e., the first PC), which means that the second and third PCs are comparable in significance (measured by the eigenvalue, which is the variance of the database samples in the given PC direction) to the first PC. In comparison, the first PC of databases 1 and 3 has significantly higher variance than the second and third PCs. This can be further confirmed from

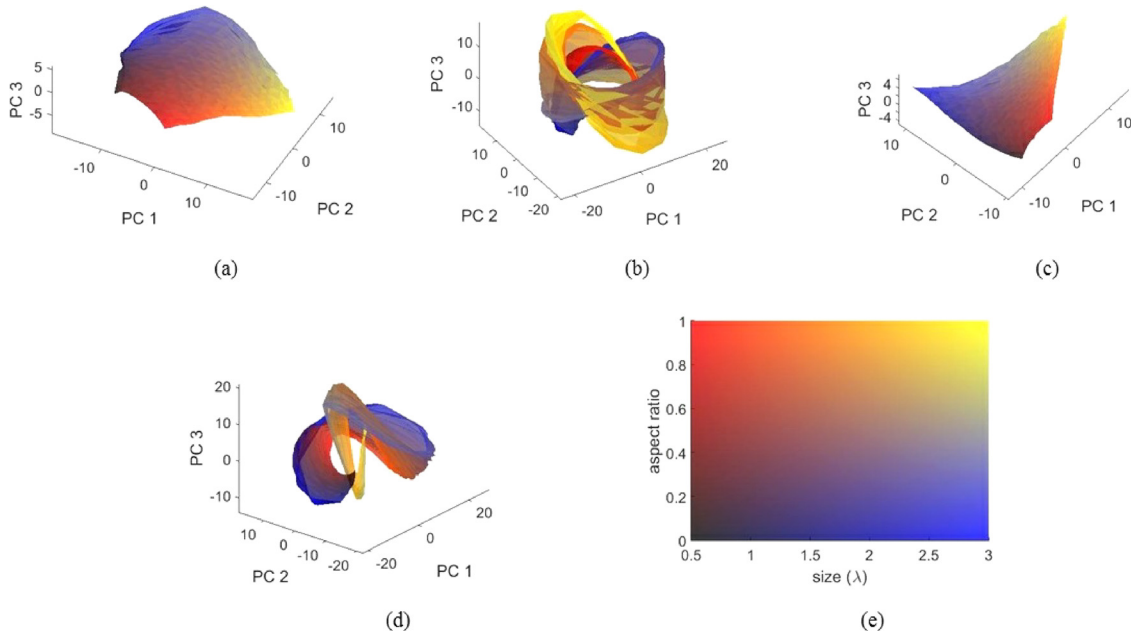

FIG. 2. (Color online) The shapes of the d-manifolds of databases 1–4 in three-dimensional pc-space (a),(b),(c),(d), and the two-dimensional parameter space (e).

the results given in Fig. 3. According to the selection criterion described above (i.e., only the PCs that have variance above the threshold are regarded as significant), the number of informative PCs is $N_1 = 8$ for database 1, $N_2 = 16$ for database 2, $N_3 = 7$ for database 3, and $N_4 = 26$ for database 4. This increase in the number of informative PCs (by including the phase and frequency information) clearly indicates the increase in the amount of useful information for defect characterisation.

B. Uncertainty analysis

In this section, the achievable characterisation accuracy of different defect databases is compared by evaluating their characterisation uncertainty. The characterisation uncertainty at a point on the d-manifold with parameter $\boldsymbol{p}_0$ can be described by the conditional probability $P(\boldsymbol{p}|\boldsymbol{P}_0)$, where $\boldsymbol{P}_0$ is the scattering matrix (in pc-space) of the reference defect with parameter $\boldsymbol{p}_0$. The calculation of $P(\boldsymbol{p}|\boldsymbol{P}_0)$ is dependent on an assumption about underlying noise distribution.[23] Here we use the general coherent noise model introduced by Velichko *et al.*[23] for the purpose of quantifying the characterisation uncertainty.

The coherent noise is modeled as a two-dimensional random Gaussian rough surface,[23] and is described by the parameters σ_{coh} [i.e., root-mean-square (RMS) amplitude of the noise], $\lambda_{\text{coh},1}$ and $\lambda_{\text{coh},2}$ (i.e., correlation lengths in θ_1 and θ_2 directions). Given these parameters, random coherent noise is obtained from

$$\boldsymbol{n} = \left(\boldsymbol{C} \otimes \boldsymbol{n}_g - \mu'\right)\frac{\sigma_{\text{coh}}}{\sigma'}, \tag{11}$$

where $\boldsymbol{C}$ denotes the correlation function and is assumed to be Gaussian, i.e., $\boldsymbol{C}(\zeta_1, \zeta_2) = \exp\left(-(\zeta_1^2/\lambda_{\text{coh},1}^2) - (\zeta_2^2/\lambda_{\text{coh},2}^2)\right)$, $\boldsymbol{n}_g$ is zero-mean, unit-variance white Gaussian random noise, and μ' and σ' are the mean and standard deviation of the convolution $\boldsymbol{C} \otimes \boldsymbol{n}_g$, respectively.[23,27] Figure 4 shows a random realisation of the coherent noise (at $f = 2.5$ MHz) with the parameters $\sigma_{\text{coh}} = 0.16$, $\lambda_{\text{coh},1} = \lambda_{\text{coh},2} = 20°$. Note that the noise standard deviation σ_{coh} is calculated from the relationship

$$\sigma_{\text{coh}}(\omega) = n_\sigma A_r(\omega), \tag{12}$$

where $n_\sigma(=5\%)$ is the noise level, and $A_r(\omega)$ is the peak amplitude of the reference scattering matrix (chosen as that of a 3λ crack here) at a given frequency (i.e., 2.5 MHz for databases 1 and 2, and between 1.5 MHz and 3.5 MHz for databases 3 and 4). Equation (12) means that the noise standard deviation is the same for databases 1 and 2, as well as the 2.5 MHz frequency component of databases 3 and 4. For example, for database 2, the noise is simulated as

$$\boldsymbol{n}^{(\text{db},2)} = \boldsymbol{n}_{\text{real}}(\omega_c) + i\boldsymbol{n}_{\text{imag}}(\omega_c), \tag{13}$$

where $\boldsymbol{n}_{\text{real}}(\omega_c)$ and $\boldsymbol{n}_{\text{imag}}(\omega_c)$ are drawn independently from the noise model given in Eq. (11) where $\sigma_{\text{coh}} = n_\sigma A_r(\omega_c) = 0.16$. For database 4, the noise is simulated as

$$\boldsymbol{n}^{(\text{db},4)} = \begin{bmatrix} \boldsymbol{n}_{\text{real}}(\omega_1) \\ \boldsymbol{n}_{\text{real}}(\omega_2) \\ \boldsymbol{n}_{\text{real}}(\omega_3) \\ \boldsymbol{n}_{\text{real}}(\omega_4) \\ \boldsymbol{n}_{\text{real}}(\omega_5) \end{bmatrix} + i \begin{bmatrix} \boldsymbol{n}_{\text{imag}}(\omega_1) \\ \boldsymbol{n}_{\text{imag}}(\omega_2) \\ \boldsymbol{n}_{\text{imag}}(\omega_3) \\ \boldsymbol{n}_{\text{imag}}(\omega_4) \\ \boldsymbol{n}_{\text{imag}}(\omega_5) \end{bmatrix}. \tag{14}$$

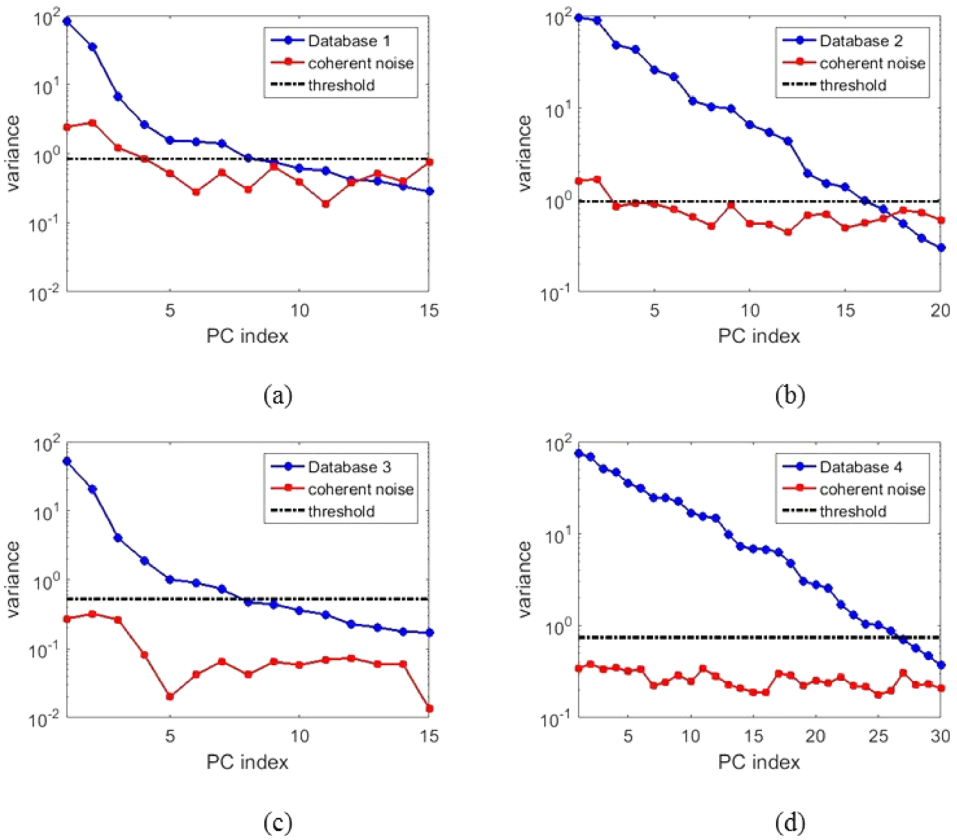

FIG. 3. (Color online) The variance of defect databases and coherent noise in different PC directions: (a)–(d) show the results of databases 1–4, respectively. The coherent noise dataset (contains 1000 random realisations of noise for each database) is simulated from the noise model given in Eq. (11), where the noise standard deviation σ_{coh} is determined from Eq. (12), and the correlation lengths are chosen to be $\lambda_{\text{coh},1} = \lambda_{\text{coh},2} = 20°$.

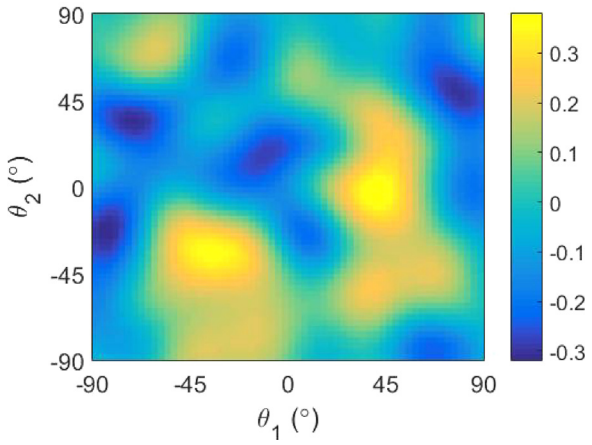

FIG. 4. (Color online) One realisation of random Gaussian coherent noise with parameters $\sigma_{\text{coh}} = 0.16$, $\lambda_{\text{coh},1} = \lambda_{\text{coh},2} = 20°$.

Similarly, $\boldsymbol{n}_{\text{real}}(\omega_i)$ and $\boldsymbol{n}_{\text{imag}}(\omega_i)$ $(i = 1, 2, 3, 4, 5)$ are drawn independently using Eq. (11). The variance of the noise data (estimated from 1000 random realisations of noise for each database) in different PC directions corresponding to databases 1–4 is shown in Fig. 3. It is observed that for the most informative PCs (i.e., the first few PCs), the signal-to-noise ratio (which is defined as the ratio of the variance of database samples to the noise variance in a given PC direction) can be increased by including the phase part of the scattering matrix. It is also interesting to note that the noise distribution is near isotropic for database 4. This effectively increases the dimensionality of the noise pc-space, which in turn results in reduced characterisation uncertainty (see the Appendix for related discussions). It is worth pointing out that when modeling multiple-frequency data, noises at different frequencies are simulated independently from the Gaussian noise model for the purpose of this paper. Future work will aim to answer more fundamental questions such as how many independent frequency components exist.

If measurement noise is described by the general coherent noise model given above, an analytic expression of the conditional probability $P(\boldsymbol{p}|\boldsymbol{P}_0)$ can be derived (see the Appendix). Figures 5(a)–5(d) show the conditional probability $P(\boldsymbol{p}|\boldsymbol{P}_0)$ [calculated using Eq. (A4), where the noise standard deviation is determined from Eq. (12) and the correlation lengths are selected to be $\lambda_{\text{coh},1} = \lambda_{\text{coh},2} = 20°$] for defect parameters $\boldsymbol{p}_0 = [2\lambda, 0.8]^T$ when databases 1–4 are used for characterisation. The physical meaning of the results shown in Fig. 5 is similar to that of the point spread function, and it describes the probability of defect parameter $\boldsymbol{p}$ given the measurement of the scattering matrix $\boldsymbol{P}_0$. It is clearly observed that by using the phase information of a scattering matrix, the characterisation uncertainty of databases 2 and 4 has become significantly lower than that of databases 1 and 3. In addition, using scattering information obtained at multiple frequencies is also shown to be beneficial, and database 4 has the lowest characterisation uncertainty for the considered defect. Figures 5(e)–5(h) show the results of another defect with parameters $\boldsymbol{p}_0 = [2.8\lambda, 0.1]^T$. Similar results are observed for this crack-like defect, which has a relatively large size and a small non-zero aspect ratio.

The same uncertainty analysis can be carried out for each of the reference defects in the database. Then, the characterisation performance of different defect databases can be compared by calculating the root-mean-square error (RMSE) of the defect parameters, which is defined as

$$\text{RMSE}(p_i) = \sqrt{\int (p_i - p_{i0})^2 P(\boldsymbol{p}|\boldsymbol{P}_0) dp}, \quad i = 1, 2, \ldots, K, \tag{15}$$

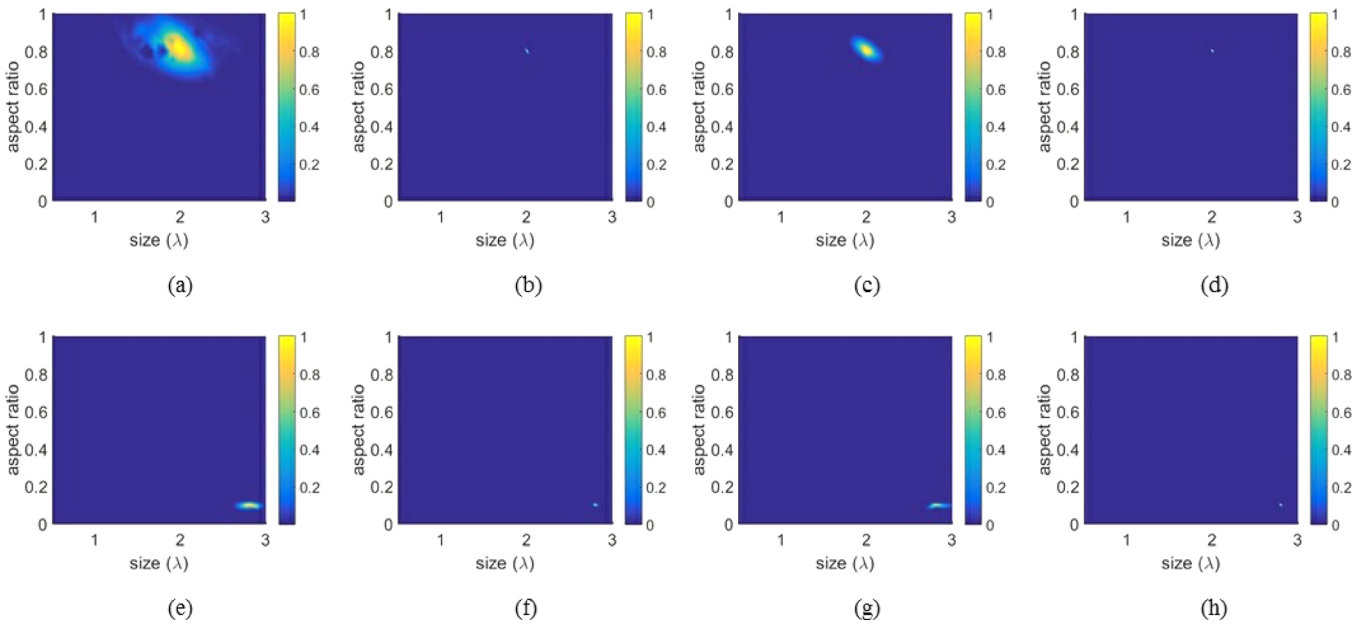

FIG. 5. (Color online) Conditional probability $P(\boldsymbol{p}|\boldsymbol{P}_0)$ [calculated using Eq. (A4)] for defect parameters $\boldsymbol{p}_0 = [2\lambda, 0.8]^T$ (a),(b),(c),(d) and $\boldsymbol{p}_0 = [2.8\lambda, 0.1]^T$ (e),(f),(g),(h), and for databases 1 (a),(e), 2 (b),(f), 3 (c),(g), and 4 (d),(h). The noise standard deviation σ_{coh} used in simulation is determined from Eq. (12), and the correlation lengths are chosen to be $\lambda_{\text{coh},1} = \lambda_{\text{coh},2} = 20°$.

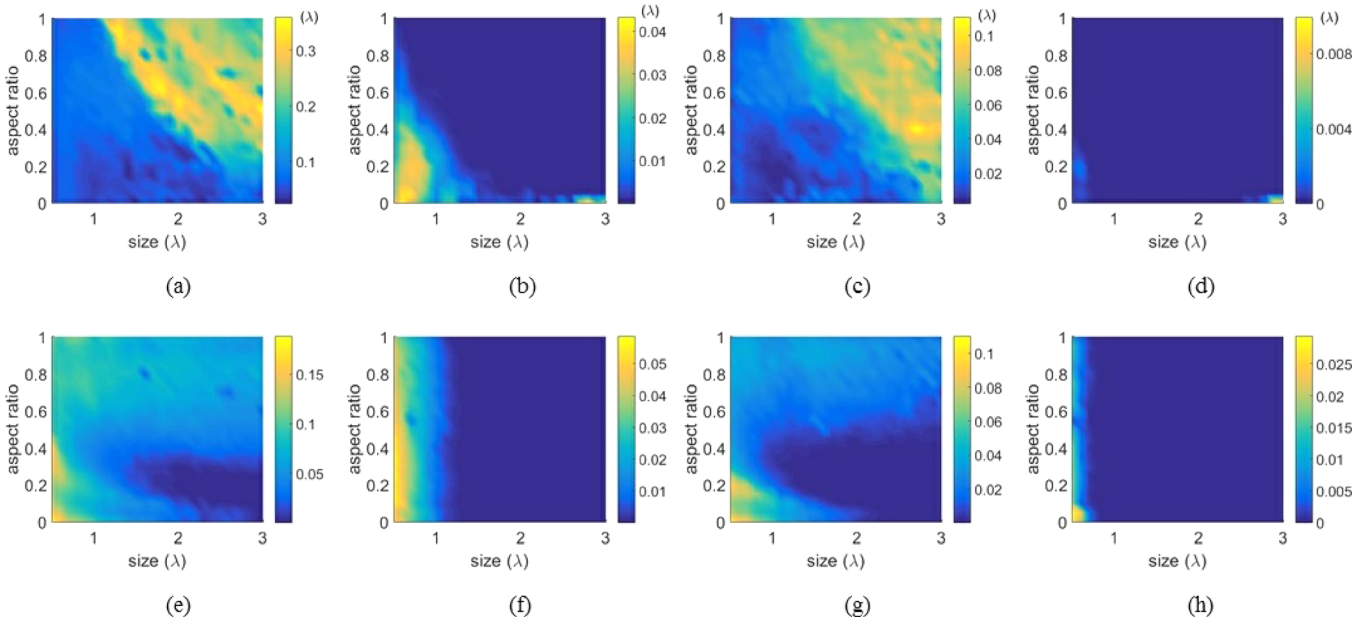

FIG. 6. (Color online) RMSE results of reference defects [calculated using Eq. (15)] in defect size (a),(b),(c),(d) and aspect ratio (e),(f),(g),(h) for databases 1 (a),(e), 2 (b),(f), 3 (c),(g), and 4 (d),(h). The same noise parameters as in Fig. 5 are used for probability density calculations.

where the vector $\boldsymbol{p}$ denotes the defect parameter, p_i is the ith component of $\boldsymbol{p}$, p_{i0} is the actual value of the ith defect parameter, and K is the number of defect parameters. In the example considered in this section, $\boldsymbol{p} = [l, r]^T$ and $K = 2$. Note that the RMSE results of defect size and aspect ratio can be used as indicators of the characterisation uncertainty at a given point on the d-manifold. The RMSE results (the conditional probability of defect parameters are calculated as described in the Appendix) are shown in Fig. 6, which are useful for determining which defect database is best suited for characterising a given defect. The advantage of databases 2 and 4 over databases 1 and 3 has been clearly demonstrated in these results. It is particularly interesting to note that the RMSE of defect size is higher for large defects (i.e., sizes above 2λ) for databases 1 and 3, and this is consistent with the results reported by Zhang *et al.* [i.e., defect characterisation based on the scattering amplitude is most effective when defect size is below 2λ (Ref. 21)]. It should be noted that the results shown in Fig. 6 are dependent on the specific noise parameters used for probability density calculations. In addition, as the range of the incident/scattering angles in the defect database decreases, the achievable characterisation performance is expected to drop.

III. THE EFFECT OF LOCALISATION ERROR ON PHASE OF THE SCATTERING MATRIX

The analysis performed in Sec. II suggests that if the phase of a scattering matrix can be measured reliably, it can be used for more accurate defect characterisation. However, the extraction of this phase information from experimental data is not straightforward since it is easily affected by small localisation errors. In this section, the effect of localisation error on the measured phase of a scattering matrix is investigated based on the notations and the coordinate system definition given in Fig. 7, which shows the ray path for a transmitter (Tx) and a receiver (Rx) element of a linear array. In Fig. 7, C denotes the actual defect location relative to which the defect scattering matrix $\boldsymbol{S}$ is defined. C' is the estimated defect location from which the scattering matrix $\boldsymbol{S}'$ is extracted. The localisation error is denoted as $\vec{r}$, and $\vec{r}_1$ and $\vec{r}_1'$ represent vectors pointing from the transmitter element to the actual and estimated defect locations, respectively. Similarly, $\vec{r}_2$ and $\vec{r}_2'$ are vectors pointing from the actual and estimated defect locations, respectively, to the receiver element. The array measurement corresponding to the considered transmitter and receiver elements can be described by the following two expressions:

$$G(x_T, x_R, \omega) = \frac{I_0(\omega)\sqrt{\lambda}}{|\vec{r}_1||\vec{r}_2|}\exp\{-ik[|\vec{r}_1| + |\vec{r}_2|]\} \times \boldsymbol{S}(\theta_1, \theta_2, \omega), \tag{16}$$

$$G(x_T, x_R, \omega) = \frac{I_0(\omega)\sqrt{\lambda}}{|\vec{r}_1'||\vec{r}_2'|}\exp\{-ik[|\vec{r}_1'| + |\vec{r}_2'|]\} \times \boldsymbol{S}'(\theta_1', \theta_2', \omega). \tag{17}$$

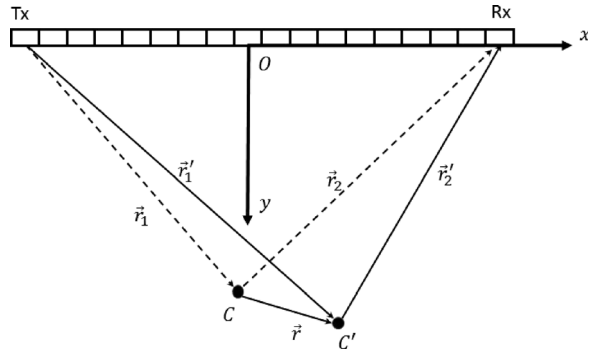

FIG. 7. The coordinate system and notations used for deriving the effect of localisation error on phase of a scattering matrix.

Equations (16) and (17) are based on the hybrid model given by Zhang *et al.*,[21] where $I_0(\omega)$ is the spectrum of input signal, $k = \omega/c$ is the ultrasonic wavenumber, and θ_1 (θ_1') and θ_2 (θ_2') are incident and scattering angles for the actual (estimated) defect location. Note here that the array elements are assumed to act as point sources and the effect of element directivity is ignored. Under the far-field assumption, we have

$$\begin{aligned}|\vec{r}_1'| &= (\vec{r}_1{}' \cdot \vec{r}_1{}')^{1/2} = [(\vec{r}_1 + \vec{r}) \cdot (\vec{r}_1 + \vec{r})]^{1/2} \\ &= \left(|\vec{r}_1|^2 + |\vec{r}|^2 + 2\vec{r}_1 \cdot \vec{r}\right)^{1/2} \\ &= |\vec{r}_1|\left(1 + \frac{|\vec{r}|^2}{|\vec{r}_1|^2} + \frac{2\vec{r}_1 \cdot \vec{r}}{|\vec{r}_1|^2}\right)^{1/2} \approx |\vec{r}_1|\left(1 + \frac{\vec{r}_1 \cdot \vec{r}}{|\vec{r}_1|^2}\right),\end{aligned} \tag{18}$$

where Taylor-series expansion[28] is applied in the last step and higher order terms are ignored since $|\vec{r}| \ll |\vec{r}_1|$. Let $\vec{e}_{r1}$ be the unit vector pointing from the transmitter element to C so that $\vec{r}_1 = |\vec{r}_1| \cdot \vec{e}_{r1}$, then Eq. (18) becomes

$$|\vec{r}_1'| \approx |\vec{r}_1| + \vec{r} \cdot \vec{e}_{r1}. \tag{19}$$

Similarly, we have

$$|\vec{r}_2'| \approx |\vec{r}_2| - \vec{r} \cdot \vec{e}_{r2}, \tag{20}$$

where $\vec{e}_{r2}$ is the unit vector pointing from C to the receiver element.

From Eqs. (19) and (20) and the fact that $|\vec{r}| \ll |\vec{r}_1|$, $|\vec{r}| \ll |\vec{r}_2|$, we have

$$|\vec{r}_1'||\vec{r}_2'| \approx |\vec{r}_1||\vec{r}_2|, \quad \theta'_1 \approx \theta_1, \quad \theta'_2 \approx \theta_2. \tag{21}$$

Finally, from Eqs. (16)–(21), we conclude that

$$\boldsymbol{S}' = \boldsymbol{S} \times \exp[ik\vec{r} \cdot (\vec{e}_{r1} - \vec{e}_{r2})]. \tag{22}$$

Equation (22) means that if the localisation error $|\vec{r}|$ is small, then its effect on the amplitude of the scattering matrix is ignorable. However, the phase change must be accounted for even for small localisation errors since the wavenumber $k = \omega/c$ is normally very high for ultrasonic waves (e.g., $k = 2.5 \times 10^3$ for waves propagating in aluminum when the frequency is 2.5 MHz).

Figure 8(a) shows the phase of a simulated elliptical defect with parameters $\boldsymbol{p} = [1\lambda, 0.2]^T$ at two diagonal components of the scattering matrix $\theta_2 = \theta_1$ and $\theta_2 = -\theta_1$, which is extracted assuming that the actual defect location (i.e., the geometric centre of the ellipse) is known. Figures 8(b) and 8(c) show the same phase results extracted with localisation errors of -0.2λ in y axis and 0.2λ in x axis, respectively. In Fig. 8(b), although phase in both diagonal lines has changed compared to the result obtained with no localisation error, it is noted that the difference between the two diagonal lines remains unchanged. This can be explained using Eq. (22). Suppose $\Phi(\theta_{\text{in}}, \theta_{\text{sc}})$ denotes the true phase of the scattering coefficient $S(\theta_{\text{in}}, \theta_{\text{sc}})$. If the estimated defect location has a localisation error $\vec{r}$, the measured phase becomes

$$\Phi'(\theta_{\text{in}}, \theta_{\text{sc}}) = \Phi(\theta_{\text{in}}, \theta_{\text{sc}}) + k\vec{r} \cdot (\vec{e}_{r1} - \vec{e}_{r2}), \tag{23}$$

where as before, $\vec{e}_{r1}$ and $\vec{e}_{r2}$ are unit vectors corresponding to the ray paths of incident and scattering waves. If we consider the phase $\Phi(\theta_{\text{in}}, -\theta_{\text{sc}})$ of the scattering coefficient $S(\theta_{\text{in}}, -\theta_{\text{sc}})$, the measured phase becomes (under the same localisation error $\vec{r}$)

$$\Phi'(\theta_{\text{in}}, -\theta_{\text{sc}}) = \Phi(\theta_{\text{in}}, -\theta_{\text{sc}}) + k\vec{r} \cdot (\vec{e}_{r1} - \vec{e}_{r3}), \tag{24}$$

where $\vec{e}_{r3}$ is the unit vector corresponding to the ray path of the scattering wave for which the scattering angle is $-\theta_{\text{sc}}$. If the localisation error is in y axis, it is easy to verify that $\vec{r} \cdot \vec{e}_{r2} = \vec{r} \cdot \vec{e}_{r3}$ [see Fig. 9(a)], based on which we have the relationship

$$\Phi'(\theta_{\text{in}}, \theta_{\text{sc}}) - \Phi'(\theta_{\text{in}}, -\theta_{\text{sc}}) = \Phi(\theta_{\text{in}}, \theta_{\text{sc}}) - \Phi(\theta_{\text{in}}, -\theta_{\text{sc}}). \tag{25}$$

Equation (25) means that the phase difference of two scattering coefficients is a constant if they are defined for the same incident angle θ_{in} and scattering angles that have the relationship $\theta_{sc1} + \theta_{sc2} = 0$. Note that the result shown in Fig. 8(b) is for the case when $\theta_{\text{sc1}} = \theta_{\text{in}}$ and $\theta_{\text{sc2}} = -\theta_{\text{in}}$.

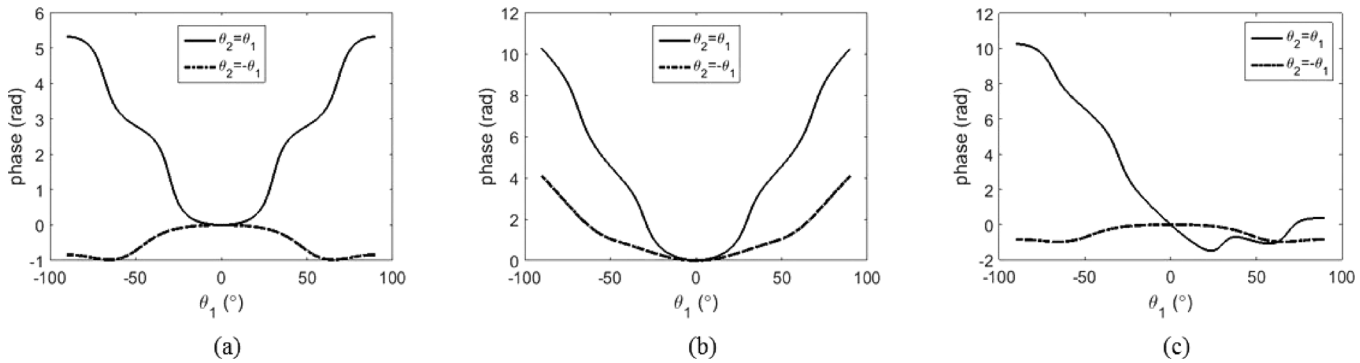

FIG. 8. Phase of a simulated elliptical defect with parameters $\boldsymbol{p} = [1\lambda, 0.2]^T$ at two diagonal components of the scattering matrix $\theta_2 = \theta_1$ and $\theta_2 = -\theta_1$, where (a) extracted at the actual defect location (i.e.,. the geometric centre of the ellipse), (b) extracted with a localisation error of -0.2λ in y axis, and (c) extracted with a localisation error of 0.2λ in x axis. The phase results shown here are unwrapped and are relative to the phase of the specular reflection coefficient (i.e., $\theta_1 = \theta_2 = 0°$).

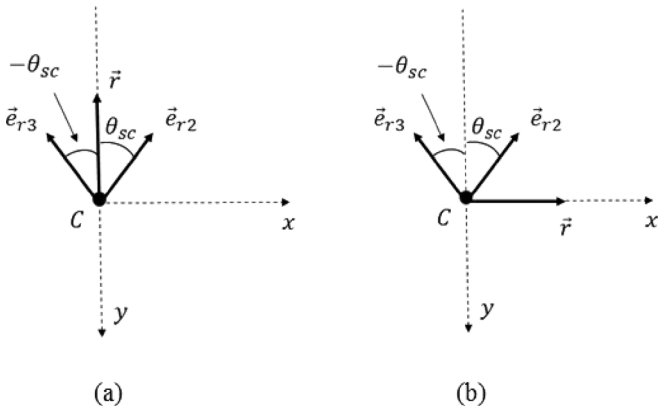

FIG. 9. Unit vectors corresponding to ray paths of the scattering waves for which the scattering angles are θ_{sc} and $-\theta_{sc}$: (a) localisation error is in y axis, and (b) localisation error is in x axis.

If the localisation error $\vec{r}$ is in x axis, we have $\vec{r} \cdot \vec{e}_{r2} = -\vec{r} \cdot \vec{e}_{r3}$ [see Fig. 9(b)], which means that the relationship given in Eq. (25) is no longer valid when the localisation error $\vec{r}$ has a non-zero component in x axis. It is observed from Fig. 8(c) that phases in $\theta_2 = -\theta_1$ are unchanged [this can also be verified from Eq. (22)], but the phase range (i.e., maximum phase minus minimum phase after the phase is unwrapped) in $\theta_2 = \theta_1$ has become larger. As can be seen, the pulse-echo phase changes in opposite directions for $\theta_{\text{in}} < 0$ and $\theta_{\text{in}} > 0$, and the phase range is minimum when there is no localisation error in x axis. This is true for all of the database defects (i.e., cracks and elliptical voids oriented at 0°), because they have symmetrical shapes and the pulse-echo phase is symmetrical about $\theta_{\text{in}} = 0°$ when there is no localisation error. Based on this observation, the x coordinate of the defect location can be determined to be the location at which the range of the experimentally measured pulse-echo phase is minimised. Note that this approach can also be generalised to characterise any type of defect (e.g., defects which have irregular shapes and/or non-zero orientation angles) by applying the same pre-processing (i.e., minimising the range of the pulse-echo phase) to both the experimental data and the database.

In practical situations, the measurable incident/scattering angles are limited to some angular range, which may not be symmetrical about $\theta = 0°$. However, the idea of extracting the phase difference (instead of the exact phase values) can still be adopted. Figure 10(a) shows an illustration of this. The global coordinate system is defined by the array, and the defect location C is not aligned with the array centre O. Assume that unit vectors $\vec{e}_{r2}$ and $\vec{e}_{r3}$ correspond to ray paths of the first and last array elements from the defect. Based on this, we have $\vec{r} \cdot \vec{e}_{r2} = \vec{r} \cdot \vec{e}_{r3}$ if the localisation error $\vec{r}$ is in y' axis, which corresponds to the $\vec{e}_{r2} + \vec{e}_{r3}$ direction. Hence, the phase difference can be calculated in a similar manner as described above, and the defect location in x' axis, which is perpendicular to the y' direction, can be determined by minimising the range of the pulse-echo phase as before. Figure 10(b) shows the phase range (in $\theta_2 = \theta_1$) of a simulated ellipse with parameters $\boldsymbol{p} = [1\lambda, 0.2]^T$, which is obtained at different extraction centres in x' axis. When the

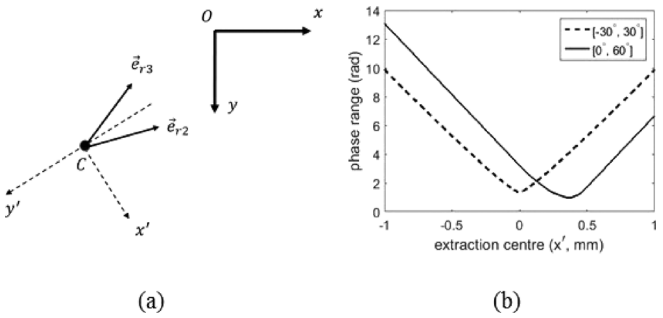

FIG. 10. (a) The defect coordinate system used for calculating the phase difference, and (b) phase range (in $\theta_2 = \theta_1$) of a simulated elliptical defect with parameters $\boldsymbol{p} = [1\lambda, 0.2]^T$ obtained at different extraction centres in x' axis, when the measured angular ranges are $[-30°, 30°]$ and $[0°, 60°]$.

measured incident/scattering angles are within $[-30°, 30°]$, the minimum phase range is achieved at $x' = 0$ as explained above. This means that the extraction centre obtained with the proposed approach is the actual defect location when the measurable incident/scattering angles are symmetrical about $\theta = 0°$. However, if the measurable incident/scattering angles are not symmetrical about $\theta = 0°$ (e.g., are within $[0°, 60°]$), the extraction centre can potentially be different from the actual defect location.

IV. EXPERIMENTS

Characterisation results obtained from experimental data measured on an aluminum test specimen containing nine machined elliptical defects (see Fig. 11) are discussed in this section. Measurements were performed using a 2.5 MHz, 64 element array with the element pitch of 0.5 mm, and the test configuration shown in Fig. 1 was adopted. The defects are described using three parameters: size l, aspect ratio r, and orientation angle θ, and the actual parameter values of ellipses 1–9 are given in Table I. The considered parameter ranges of the defect database are $[0.5\lambda, 3\lambda]$ for the size (sampled in 0.1λ intervals), [0,1] for the aspect ratio (sampled in 0.05 intervals), and $[-80°, 80°]$ for the orientation angle (measured with respect to the array direction, is positive if measured clockwise, and is sampled in 5° intervals).

As in Sec. II, four different versions of the defect database are compared. Databases 1–4 are prepared according to Eqs. (2)–(6), but the phase term $\Phi[\boldsymbol{S}(\theta_{\text{in}}, \theta_{\text{sc}})]$ is replaced by $\Phi[\boldsymbol{S}(\theta_{\text{in}}, \theta_{\text{sc}})] - \Phi[\boldsymbol{S}(\theta_{\text{in}}, -\theta_{\text{sc}})]$ as the latter is invariant to the localisation error in y axis, considering the fact that the

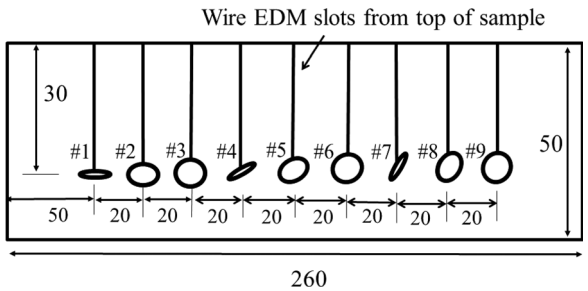

FIG. 11. (Dimensions are in millimeters.) Experimental sample geometries containing elliptical defects.

TABLE I. Defect parameters of ellipses 1–9 shown in Fig. 11 ($\lambda = 2.5$ mm is the ultrasonic wavelength at the centre frequency $f = 2.5$ MHz).

	Parameters		
Ellipse	Aspect ratio	Size (λ)	Angle (°)
1	0.32	1.00	0
2	0.50	1.00	0
3	0.80	1.00	0
4	0.32	1.00	30
5	0.50	1.00	30
6	0.80	1.00	30
7	0.32	1.00	60
8	0.50	1.00	60
9	0.80	1.00	60

target defect is located at the array centre and the measured scattering matrices cover the incident/scattering angles that are symmetrical about $\theta = 0°$. Moreover, the extraction centre in x axis is searched for (by minimising the range of the pulse-echo phase) within ± 1 mm region from the defect indication in the image (corresponding to the peak intensity point). The database scattering matrices are pre-processed in the same way—for angled defects, this means that the extraction centre can potentially be different from the actual defect location, and defects having an orientation angle of 0° are unaffected.

Figures 12(a) and 12(b) show the real and imaginary parts, respectively, of the experimentally measured scattering matrix of ellipse 5 at $f = 2.5$ MHz, and Figs. 12(c) and 12(d) are the real and imaginary parts, respectively, of the database scattering matrix with parameters $\boldsymbol{p} = [l, r, \theta]^T = [1\lambda, 0.5, 30°]^T$. The experimental scattering matrices are extracted using the inverse imaging approach,[29] and it is clearly seen that both the real and imaginary parts of the scattering matrix have been extracted to high accuracy (e.g., the correlation coefficient between the experimental measurement and the modeled result is 0.97 for the real part and 0.96 for the imaginary part).

Given these experimental data, the characterisation result can be obtained as the conditional probability $P(\boldsymbol{p}|\boldsymbol{P}_{\text{exp}})$ where $\boldsymbol{P}_{\text{exp}}$ is the experimentally measured scattering matrix in pc-space. Figure 13 shows the three-dimensional probability maps of ellipses 5 and 7 obtained for databases 1–4, where Eq. (A4) is adopted for probability density calculations. For each defect database, the noise parameter σ_{coh} is set to be the same as the maximum standard deviation of the measurement noise (calculated by assuming that the actual defect parameters are known). Then, the correlation lengths $\lambda_{\text{coh},1}$ and $\lambda_{\text{coh},2}$ are obtained using the maximum-likelihood estimation method (see the Appendix). The noise parameters used for probability density calculations are $\sigma_{\text{coh}} = 0.06$, $\lambda_{\text{coh},1} = 40°$, $\lambda_{\text{coh},2} = 35°$ for database 1, $\sigma_{\text{coh}} = 0.09$, $\lambda_{\text{coh},1} = 50°$, $\lambda_{\text{coh},2} = 20°$ for database 2, $\sigma_{\text{coh}} = 0.11$, $\lambda_{\text{coh},1} = 60°$, $\lambda_{\text{coh},2} = 5°$ for database 3, and $\sigma_{\text{coh}} = 0.09$, $\lambda_{\text{coh},1} = 20°$, $\lambda_{\text{coh},2} = 40°$ for database 4. It is seen from the results shown in Fig. 13 that the characterisation uncertainty can be significantly reduced by using databases 3 and 4 (i.e., by using phase and multiple-frequency data), and this is due to the increased dimensionality of the noise pc-space as explained in Sec. II. Compared to databases 1 and 3, the main advantage of databases 2 and 4 is shown to be the reduced uncertainty in defect size. As expected, the best characterisation performance is achieved by using database 4—the true parameter points are close to the maximum probability points (see Table II) and the characterisation uncertainty is low for all three defect

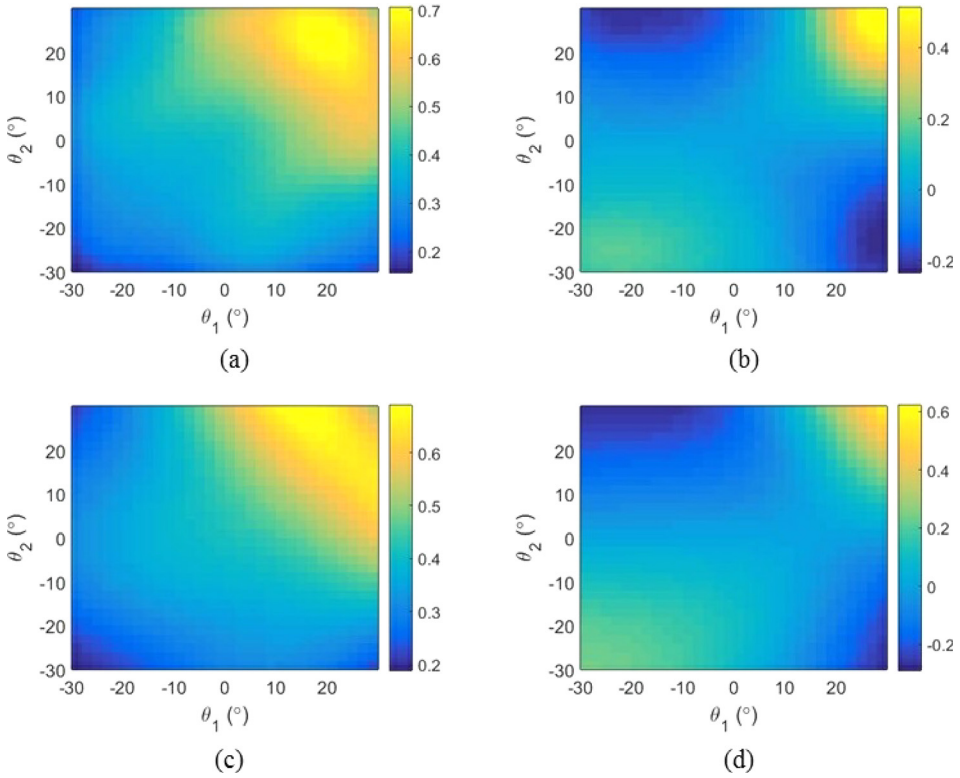

FIG. 12. (Color online) Real (a),(c) and imaginary (b),(d) parts of the scattering matrix of ellipse 5 measured experimentally (a),(b) and obtained in simulation (c),(d).

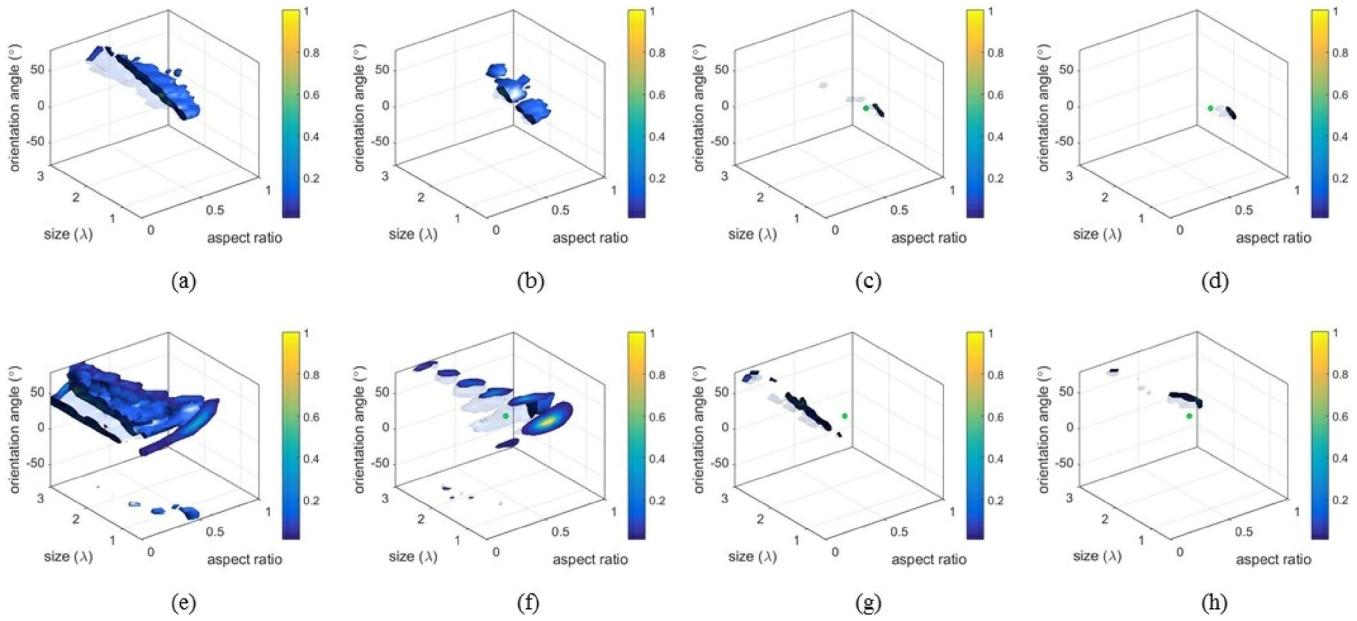

FIG. 13. (Color online) Probability maps of ellipses 5 (a),(b),(c),(d) and 7 (e),(f),(g),(h) for databases 1 (a),(e), 2 (b),(f), 3 (c),(g), and 4 (d),(h). The probabilities are normalised to the maximum value in each figure, and the green dots indicate the actual parameter values.

parameters. These findings can be further confirmed by the RMSE results of the defect parameters [calculated using Eq. (15)] given in Table III. Although database 1 gives low characterisation uncertainty in defect size for ellipses 1 and 2 (which are favourably oriented), the uncertainty in defect size is normally very high for other defects. By using database 4, the reduction in the RMSE of defect size is between 28.57% (ellipse 2) and 90.60% (ellipse 4) when compared to the results obtained with database 1. The uncertainty in aspect ratio is generally low for all the defect databases (in particular, databases 3 and 4). Moreover, defects with high aspect ratios are shown to have high uncertainty in their orientation angle results. This is because of the fact that the scattering matrix becomes insensitive to the orientation angle as the defect aspect ratio approaches 1.[23]

V. CONCLUSIONS

The possibility of using the phase and frequency information of a scattering matrix for defect characterisation is explored in this paper. It was first shown using ideal measurement scenarios where the full angular range of the scattering matrix is accessible that by including the phase, the achievable characterisation accuracy can be improved. This is due to the increased number of informative PCs and higher signal-to-noise ratios in the PC-directions. In addition, it was concluded that using the scattering matrix obtained at multiple frequencies is also beneficial to the characterisation performance.

The characterisation uncertainty for a given defect parameter $\boldsymbol{p}_0$ can be evaluated from the conditional probability $P(\boldsymbol{p}|\boldsymbol{P}_0)$ where $\boldsymbol{P}_0$ is the noise-free scattering matrix of the reference defect with parameter $\boldsymbol{p}_0$. The interpretation of the probability $P(\boldsymbol{p}|\boldsymbol{P}_0)$ is similar to that of the point spread function, and it was shown that the characterisation uncertainty can be significantly reduced by using the phase and frequency information.

Although the phase of a scattering matrix carries additional information that is useful for more accurate characterisation, it is difficult to measure in practice since it is very sensitive to

TABLE II. Characterisation results (size l, aspect ratio r, and orientation angle θ corresponding to the maximum probability point) of ellipses 1–9 shown in Fig. 11.

	Database 1			Database 2			Database 3			Database 4		
Ellipse	l (λ)	r	θ (°)	l (λ)	r	θ (°)	l (λ)	r	θ (°)	l (λ)	r	θ (°)
1	1.20	0.40	0	1.10	0.35	0	0.80	0.30	0	1.10	0.40	0
2	1.10	0.45	5	1.10	0.55	5	0.80	0.50	5	1.10	0.50	5
3	1.80	0.70	70	1.30	0.80	40	0.80	0.80	30	1.80	0.85	75
4	3.00	0.20	40	1.00	0.30	30	0.70	0.30	35	0.90	0.40	30
5	1.40	0.45	40	1.60	0.45	40	0.70	0.50	40	0.80	0.60	25
6	1.80	0.70	75	1.70	0.75	75	0.50	0.95	20	0.90	0.85	10
7	2.80	0.15	50	0.50	0.50	55	1.60	0.15	70	1.00	0.40	80
8	2.40	0.30	60	0.50	0.60	40	0.80	0.40	60	1.20	0.55	70
9	2.70	0.45	75	0.90	0.80	70	0.50	0.90	75	0.80	0.95	60

TABLE III. RMSE results of defect parameters (size l, aspect ratio r, and orientation angle θ) for ellipses 1–9 shown in Fig. 11.

	Database 1			Database 2			Database 3			Database 4		
Ellipse	l (λ)	r	θ (°)	l (λ)	r	θ (°)	l (λ)	r	θ (°)	l (λ)	r	θ (°)
1	0.19	0.08	0.62	0.16	0.12	1.25	0.20	0.02	0	0.10	0.08	0
2	0.14	0.05	4.99	0.27	0.11	10.72	0.20	0	5.00	0.10	0	5.00
3	0.94	0.14	64.65	0.52	0.13	50.96	0.25	0.03	27.88	0.54	0.07	46.37
4	1.17	0.08	6.88	0.19	0.04	2.73	0.74	0.07	5.92	0.11	0.10	0.04
5	0.92	0.08	14.59	0.51	0.05	11.39	0.34	0.06	11.70	0.21	0.11	4.96
6	0.92	0.15	54.37	0.71	0.11	45.85	0.48	0.15	30.70	0.13	0.06	20.94
7	1.02	0.16	17.32	0.55	0.12	16.22	0.91	0.16	6.81	0.57	0.08	18.61
8	0.95	0.15	11.67	0.64	0.11	13.72	0.83	0.20	3.41	0.40	0.10	10.70
9	0.86	0.20	79.33	0.72	0.18	62.12	0.44	0.10	18.07	0.23	0.16	59.42

localisation errors. The effect of the localisation error on the extracted phase was investigated, and an effective approach to reliably extracting this phase information is proposed. More specifically, it was shown that by replacing the phase term $\Phi[\boldsymbol{S}(\theta_{\text{in}}, \theta_{\text{sc}})]$ with $\Phi[\boldsymbol{S}(\theta_{\text{in}}, \theta_{\text{sc}})] - \Phi[\boldsymbol{S}(\theta_{\text{in}}, -\theta_{\text{sc}})]$, the new phase measure (i.e., the phase difference) is invariant to localisation error in y axis. The new phase measure is still subject to the choice of the extraction centre in x axis, which can be searched for in the vicinity of the defect indication in the image by minimising the range of the pulse-echo phase.

Experimentally, nine machined elliptical defects of the size 1λ were characterised using scattering matrix databases with and without phase. It was shown that the characterisation uncertainty can also be significantly reduced by using the multiple-frequency scattering data. However, the uncertainty in defect size remains high if only the scattering amplitude is used, and the best characterisation results are obtained with the database including both the real and imaginary parts of the scattering matrix at multiple frequencies.

ACKNOWLEDGMENTS

This work was funded by the Engineering and Physical Sciences Research Council (UK, EPSRC) under Grant No. EP/L022125/1. Data necessary to support the conclusions are included in the paper.

APPENDIX: PROBABILITY DENSITY FUNCTION OF GAUSSIAN COHERENT NOISE

For completeness of the paper, some of the key results which were included in the authors' recent publication and are used extensively in this paper are briefly summarised here. Interested readers are referred to Ref. 23 for more detailed description of the defect characterisation approach using the defect manifold.

The characterisation uncertainty given some measurement $\boldsymbol{P}_{\text{exp}}$ can be evaluated by the conditional probability $P(\boldsymbol{p}|\boldsymbol{P}_{\text{exp}})$. According to Bayes' theorem, $P(\boldsymbol{p}|\boldsymbol{P}_{\text{exp}})$ can be written in the form

$$P(\boldsymbol{p}|\boldsymbol{P}_{\text{exp}}) = \frac{P(\boldsymbol{P}_{\text{exp}}|\boldsymbol{p})P(\boldsymbol{p})}{P(\boldsymbol{P}_{\text{exp}})}. \tag{A1}$$

In Eq. (A1), the probabilities $P(\boldsymbol{p})$ and $P(\boldsymbol{P}_{\text{exp}})$ are the prior probabilities of defect parameter $\boldsymbol{p}$ and scattering matrix $\boldsymbol{P}$, and without *a priori* information on the nature of a defect, it is reasonable to assume that they are constant (i.e., the defect parameter and the scattering matrix are uniformly distributed). Then, it follows that

$$P(\boldsymbol{p}|\boldsymbol{P}_{\text{exp}}) = CP(\boldsymbol{P}_{\text{exp}}|\boldsymbol{p}), \tag{A2}$$

where the normalisation constant C can be obtained from $C = (\int P(\boldsymbol{P}_{\text{exp}}|\boldsymbol{p})\,dp)^{-1}$. The characterisation uncertainty is evaluated by calculating the conditional probability $P(\boldsymbol{p}|\boldsymbol{P}_{\text{exp}})$ for each defect parameter $\boldsymbol{p}$, and using the relationship given in Eq. (A2), this can be achieved by calculating the probability $P(\boldsymbol{P}_{\text{exp}}|\boldsymbol{p})$, which is expressed in the form

$$P(\boldsymbol{P}_{\text{exp}}|\boldsymbol{p}) = P(\boldsymbol{P}_p + \boldsymbol{n}^{(\text{pc})}|\boldsymbol{p}) = P(\boldsymbol{n}^{(\text{pc})}|\boldsymbol{p}). \tag{A3}$$

In Eq. (A3), $\boldsymbol{P}_p$ is the noise-free scattering matrix of the defect with parameter $\boldsymbol{p}$. Hence, the term $P(\boldsymbol{n}^{(\text{pc})}|\boldsymbol{p})$, which describes the underlying noise distribution for defect parameter $\boldsymbol{p}$, has a key impact on the characterisation uncertainty. For simplicity, it is further assumed that the noise distribution is independent of defect parameter $\boldsymbol{p}$ in this paper.

It is shown in Eq. (11) that random Gaussian coherent noise $\boldsymbol{n}$ follows a multivariate Gaussian distribution. Since PCA is a linear operation, the noise term $\boldsymbol{n}^{(\text{pc})}$ in defect pc-space also has multivariate normality. If we transform $\boldsymbol{n}^{(\text{pc})}$ into the noise pc-space by applying the same procedure as described in Eqs. (8)–(10), the noise components in this noise pc-space become independent since their covariance matrix is diagonal.[23] As a result, the noise distribution can be written as

$$P\left(\boldsymbol{n}^{(\text{pc})}|\sigma_{\text{coh}}, \lambda_{\text{coh},1}, \lambda_{\text{coh},2}\right) = \frac{1}{(2\pi)^{N_s/2}|\boldsymbol{D}_{\text{coh}}|^{1/2}} \exp\left(-\frac{1}{2}\boldsymbol{n}^{(\text{pc})T}\boldsymbol{V}_{\text{coh}}\boldsymbol{D}_{\text{coh}}^{-1}\boldsymbol{V}_{\text{coh}}^{T}\boldsymbol{n}^{(\text{pc})}\right), \tag{A4}$$

where N_s denotes the dimensionality of $\boldsymbol{n}^{(\text{pc})}$, diagonal matrix $\boldsymbol{D}_{\text{coh}}$ contains the eigenvalues of the "noise database," and column vectors of the matrix $\boldsymbol{V}_{\text{coh}}$ define the coordinate axes of the noise pc-space. Note that the calculation of $\boldsymbol{D}_{\text{coh}}$

and $\boldsymbol{V}_{\text{coh}}$ is based on construction of a "noise database," and is thus related to noise parameters σ_{coh}, $\lambda_{\text{coh},1}$, and $\lambda_{\text{coh},2}$ used to simulate the noise data. This means that given some experimental measurements, the noise parameters can potentially be obtained using the maximum-likelihood estimation method. For example, suppose $\boldsymbol{n}_i^{(\text{pc})}$ $(i = 1, 2, \ldots, K)$ represent experimental noise vectors obtained from a set of measurements. Based on this, the noise parameters can be estimated as

$$\left[\tilde{\sigma}_{\text{coh}}, \tilde{\lambda}_{\text{coh},1}, \tilde{\lambda}_{\text{coh},2}\right] = \underset{[\sigma_{\text{coh}}, \lambda_{\text{coh},1}, \lambda_{\text{coh},2}]}{\text{argmax}} \sum_{i=1}^{K} \log P\left(\boldsymbol{n}_i^{(pc)} | \sigma_{\text{coh}}, \lambda_{\text{coh},1}, \lambda_{\text{coh},2}\right). \tag{A5}$$

Finally, it is worth pointing out that only the first few noise-pc components are significant (which is similar to the defect pc-space), and the noise vector $\boldsymbol{n}^{(\text{pc})}$ needs to be truncated when calculating the probability distribution using Eq. (A4).[23]

[1]J. D. Achenbach, "Quantitative nondestructive evaluation," Int. J. Solids Struct. **37**, 13–27 (2000).
[2]D. E. Bray and R. K. Stanley, *Non-Destructive Evaluation, A Tool in Design Manufacturing and Service*, revised ed. (CRC Press, Boca Raton, FL, 1997).
[3]T. Kundu, *Ultrasonic Nondestructive Evaluation: Engineering and Biological Material Characterization* (CRC Press, Boca Raton, FL, 2004).
[4]A. F. Grandt, *Fundamentals of Structural Integrity: Damage Tolerant Design and Nondestructive Evaluation* (Wiley, Hoboken, NJ, 2003).
[5]J. Blitz and G. Simpson, *Ultrasonic Methods of Non-Destructive Testing* (Chapman and Hall, London, UK, 1996).
[6]S. Baby, T. Balasubramanian, R. J. Pardikar, M. Palaniappan, and R. Subbaratnam, "Time-of-flight diffraction (TOFD) technique for accurate sizing of surface-breaking cracks," Insight **45**, 426–430 (2003).
[7]M. V. Felice, A. Velichko, and P. D. Wilcox, "Accurate depth measurement of small surface-breaking cracks using an ultrasonic array post-processing technique," NDT E Int. **68**, 105–112 (2014).
[8]B. Shakibi, F. Honarvar, M. D. C. Moles, J. Caldwell, and A. N. Sinclair, "Resolution enhancement of ultrasonic defect signals for crack sizing," NDT E Int. **52**, 37–50 (2012).
[9]L. Bai, A. Velichko, and B. W. Drinkwater, "Ultrasonic characterization of crack-like defects using scattering matrix similarity metrics," IEEE Trans. Ultrason. Ferroelectr. Freq. Control **62**, 545–559 (2015).
[10]L. Moreau, A. Hunter, A. Velichko, and P. Wilcox, "3-D reconstruction of sub-wavelength scatterers from the measurement of scattered fields in elastic waveguides," IEEE Trans. Ultrason. Ferroelectr. Freq. Control **61**, 1864–1879 (2014).
[11]L. Bai, A. Velichko, and B. W. Drinkwater, "Characterization of defects using ultrasonic arrays: A dynamic classifier approach," IEEE Trans. Ultrason. Ferroelectr. Freq. Control **62**, 2146–2160 (2015).
[12]D. K. Hsu, J. H. Rose, and D. O. Thompson, "Reconstruction of inclusions in solids using ultrasonic Born inversion," J. Appl. Phys. **55**, 162–168 (1984).
[13]B. Ma, Z. Zhou, H. Zhao, D. Zhang, and W. Liu, "Characterisation of inclusions and disbonds in honeycomb composites using non-contact non-destructive testing techniques," Insight **57**, 499–507 (2015).
[14]L. Vergara, R. Miralles, J. Gosálbez, F. J. Juanes, L. G. Ullate, J. J. Anaya, M. G. Hernández, and M. A. G. Izquierdo, "NDE ultrasonic methods to characterise the porosity of mortar," NDT E Int. **34**, 557–562 (2001).
[15]W. Punurai, J. Jarzynski, J. Qu, J. Y. Kim, L. J. Jacobs, and K. E. Kurtis, "Characterization of multi-scale porosity in cement paste by advanced ultrasonic techniques," Cement Concrete Res. **37**, 38–46 (2007).
[16]E. Eren, S. Kurama, and I. Solodov, "Characterization of porosity and defect imaging in ceramic tile using ultrasonic inspections," Ceram. Int. **38**, 2145–2151 (2012).
[17]B. W. Drinkwater and P. D. Wilcox, "Ultrasonic arrays for non-destructive evaluation: A reivew," NDT E Int. **39**, 525–541 (2006).
[18]G. D. Connolly, M. J. S. Lowe, J. A. G. Temple, and S. I. Rokhlin, "Correction of ultrasonic array images to improve reflector sizing and location in inhomogeneous materials using a ray-tracing model," J. Acoust. Soc. Am. **127**, 2802–2812 (2010).
[19]C. Holmes, B. W. Drinkwater, and P. D. Wilcox, "Post-processing of the full matrix of ultrasonic transmit-receive array data for non-destructive evaluation," NDT E Int. **38**, 701–711 (2005).
[20]N. Pörtzgen, D. Gisolf, and G. Blacquiere, "Inverse wave field extrapolation: A different NDI approach to imaging defects," IEEE Trans. Ultrason. Ferroelectr. Freq. Control **54**, 118–127 (2007).
[21]J. Zhang, B. W. Drinkwater, and P. D. Wilcox, "The use of ultrasonic arrays to characterise crack-like defecsts," J. Nondestruct. Eval. **29**, 222–232 (2010).
[22]J. Zhang, B. W. Drinkwater, and P. D. Wilcox, "Effect of roughness on imaging and sizing rough crack-like defects using ultrasonic arrays," IEEE Trans. Ultrason. Ferroelectr. Freq. Control **59**, 939–948 (2012).
[23]A. Velichko, L. Bai, and B. W. Drinkwater, "Ultrasonic defect characterisation using parametric-manifold mapping," Proc. R. Soc. A **473**, 20170056 (2017).
[24]E. Glushkov, N. Glushkova, A. Ekhlakov, and E. Shapar, "An analytically based computer model for surface measurements in ultrasonic crack detection," Wave Motion **43**, 458–473 (2006).
[25]A. Velichko and P. D. Wilcox, "A generalized approach for efficient finite element modeling of elastodynamic scattering in two and three dimensions," J. Acoust. Soc. Am. **128**, 1004–1014 (2010).
[26]I. T. Jolliffe, *Principal Component Analysis*, 2nd ed. (Springer, New York, 2002).
[27]D. J. Whitehouse, "Surface characterization and roughness measurement in engineering," Photomech. Top. Appl. Phys. **77**, 413–461 (2000).
[28]M. Abramowitz and I. A. Stegun, eds., *Handbook of Mathematical Functions: With Formulas, Graphs and Mathematical Tables* (Dover, New York, 1968).
[29]A. Velichko and P. D. Wilcox, "Reversible back-propagation imaging algorithm for postprocessing of ultrasonic array data," IEEE Trans. Ultrason. Ferroelectr. Freq. Control **56**, 2492–2503 (2009).